Check for updates

Small

NANO · MICRO small
www.small-journal.com

RESEARCH ARTICLE OPEN ACCESS

Chain Orientation and Polycrystalline Disorder as Antagonistic Descriptors of Thermal and Triboelectric Transport in 3D-Nanoconfined PMMA, PEEK, and PET Nanowire Networks

Carlos G. Cobos[1] | Miguel Ángel Tenaguillo[1] | Diego Garay-Ruiz[1] | Matthias Worgull[2] | Marc Schneider[2] | Juan P. Fernández-Blázquez[3] | Marisol Martin-Gonzalez[1]

[1]Instituto De Micro y Nanotecnología, IMN-CNM, CSIC (CEI UAM+CSIC), Tres Cantos, Spain | [2]Institute For Microstructure Technology (IMT), Karlsruhe Institute of Technology (KIT), Karlsruhe, Germany | [3]IMDEA Materials Institute, Getafe, Spain

Correspondence: Marisol Martin-Gonzalez (Marisol.martin@Csic.es)

Received: 4 June 2026 | **Revised:** 2 September 2026 | **Accepted:** 25 September 2026

Keywords: 3D anodic aluminum oxide | 3D nanoporous alumina | chain orientation | multifunctional energy materials | nanoconfinement | polymer thermal conductivity | triboelectric nanogenerator

ABSTRACT

Triboelectric nanogenerators (TENGs) require polymers that dissipate frictional heat while retaining interfacial charge, yet the microstructural rules governing both functions remain unclear, including whether polymer thermal conductivity is governed primarily by crystallinity or by chain orientation and disorder. Here, interconnected 3D anodic alumina (3D-AAO) templates provide a common nanoconfinement platform for PMMA, PEEK, and PET. 2D-WAXS reveals amorphous PMMA, PEEK that crystallizes from a fully amorphous bulk to 67.8% crystallinity but remains azimuthally disordered, and strongly oriented PET (Hermans factor $f_c = 0.915$) with a modest crystallinity increase (69.98 → 74.10%). PET reaches the highest effective-medium-derived polymer thermal conductivity (1.17 $W \cdot m^{-1} \cdot K^{-1}$), whereas PEEK shows no resolved thermal enhancement despite its high crystallinity. Amorphous PMMA shows the largest relative thermal-conductivity increase (+350%), evidencing confinement-related contributions independent of crystallization. Triboelectricity follows a contrasting trend: polycrystalline PEEK shows the largest relative enhancement (+365%), while PMMA delivers the highest absolute power density (19.71 $\mu W \cdot cm^{-2}$). An Efficiency–Orientation Model phenomenologically captures the role of crystalline texture, revealing distinct and potentially competing microstructural descriptors for thermal and triboelectric performance. These results suggest that crystalline texture and disorder, not crystalline fraction alone, should be considered when designing nanoconfined polymers for thermally managed TENGs.

1 | Introduction

Triboelectric nanogenerators (TENGs) are a promising technology for harvesting mechanical energy from ambient motion, enabling self-powered wearables, structural health monitoring, and distributed sensing platforms. However, their widespread deployment is severely limited by a fundamental thermal bottleneck: most triboelectric polymers exhibit intrinsically low thermal conductivity, so repetitive friction, accumulated surface charge, and cyclic deformation generate heat faster than it can be dissipated [1–3]. This self-heating leads to temperature-dependent degradation of the triboelectric coefficient, increased phonon scattering in the rigid amorphous fraction, and accelerated mechanical fatigue at the interfaces, ultimately reducing

This is an open access article under the terms of the Creative Commons Attribution-NonCommercial-NoDerivs License, which permits use and distribution in any medium, provided the original work is properly cited, the use is non-commercial and no modifications or adaptations are made.
© 2026 The Author(s). *Small* published by Wiley-VCH GmbH

output and device lifetime [4, 5]. Despite extensive work on surface texturing and nanofiller addition to boost power density, these approaches often neglect heat management and can even exacerbate thermal accumulation or promote electrical leakage, leaving the underlying structure–property relations between nanoconfined polymer architecture, thermal transport, and triboelectric performance largely unexplored. Because both heat dissipation and charge storage are governed by nanometer-scale morphology and interfaces, architectures based on nanoconfined polymers and high-surface-area templates are particularly appealing to control these competing processes in triboelectric nanogenerators. Conventional triboelectric polymers (poly (methyl methacrylate) (PMMA), Polydimethylsiloxane (PDMS), polytetrafluoroethylene (PTFE)) exhibit poor thermal conductivity ($\kappa \approx$ 0.1 – 0.3 $W \cdot m^{-1} \cdot K^{-1}$) [6], allowing heat to accumulate faster than it dissipates.

A parallel body of work on polymer thermal transport has established that nanoconfinement and chain alignment can dramatically enhance thermal conductivity in otherwise low-κ polymers [7, 8], yet the relative importance of crystallinity and chain orientation remains under debate. Other models such as the Ma–Tian [9] framework primarily attribute thermal conductivity to bond strength and crystalline fraction, effectively treating crystalline order as a scalar quantity without distinguishing between randomly oriented crystals and uniaxially aligned domains. More recent experimental and theoretical studies suggest a different picture: extended, well-aligned polymer chains can approach a large fraction of the crystalline thermal conductivity [10], while high crystallinity with substantial paracrystalline disorder and misoriented lamellae still yields poor heat transport [11, 12]. However, a systematic comparison of crystallinity, chain orientation (e.g., via the Hermans factor (f_c)), and interfacial disorder in identical nanoconfined architectures across multiple polymer systems is still missing, preventing the formulation of reliable design rules for thermally managed polymer devices. Nanoconfined polymer nanowires in anodic alumina templates are, in principle, ideal platforms to separate these contributions, yet previous studies have typically focused on crystallinity and crystal orientation in a single polymer or geometry, without simultaneously quantifying crystallinity, chain orientation, and interphase quality across different polymers within the same nanoarchitecture.

At the same time, the mechanisms of triboelectric charge generation in polymer–polymer contact are increasingly understood to depend sensitively on molecular and microstructural details [13]. Rather than simple electron transfer between surfaces, recent studies indicate that heterolytic covalent bond scission and material transfer dominate charge production, with the ease of bond breaking controlled by local mechanical cohesion, chain packing, and interfacial structure [14]. Polycrystalline disorder, grain boundaries, and heterogeneous interfaces can reduce mechanical strength and create abundant charge-trapping sites, en chancing triboelectric output, whereas highly ordered crystalline domains may resist bond cleavage and facilitate charge dissipation. The orientation of polymer chains relative to the contact interface can additionally influence charge transport and recombination, raising the possibility that structural motifs favorable for thermal conductivity may not be equally favorable for triboelectric performance, and vice versa [15]. Yet, a unified framework linking nanoconfined polymer structure to both thermal and triboelectric behavior in a single platform has not been demonstrated. These observations suggest that nanoconfined polymer architectures with tunable crystalline order and interfacial disorder are uniquely suited to expose such antagonistic structure–property relationships in a controlled manner.

In this work, ordered 3D anodic alumina oxide (3D-AAO) templates and hot-embossing infiltration are used to fabricate completely pore-filled poly (methyl methacrylate) (PMMA), Polyether ether ketone (PEEK), and polyethylene terephthalate (PET) nanowire arrays, in which crystallinity, chain orientation, and polycrystalline disorder can be tuned and quantified within a common nanoarchitecture. 2D Wide-Angle X-ray Scattering (WAXS) reveals that PET attains nearly perfect uniaxial chain alignment (Hermans orientation factor $f_c \approx$ 0.915) with only a modest crystallinity increase, whereas PEEK reaches high crystallinity (67.8%) but remains strongly polycrystalline and azimuthally disordered, and PMMA serves as an amorphous control. Picosecond thermoreflectance and triboelectric measurements on these identical 3D architectures show that PET exhibits the highest absolute EMT-extracted polymer thermal conductivity, whereas PMMA exhibits the largest relative thermal conductivity increase compared with its own bulk reference; PEEK exhibits the largest relative triboelectric enhancement. Here we use 3D-nanoconfined PMMA, PEEK, and PET nanowire arrays in ordered anodic alumina templates as a single platform to compare how chain orientation, crystallinity, and polycrystalline disorder correlate with both thermal and triboelectric behavior. We formulate an Efficiency–Orientation Model as a phenomenological framework to discuss how crystalline texture may influence the experimentally observed conductivities.

2 | Results and Discussion

The innovative pulsed anodization process in oxalic acid generates 3D-AAO templates with longitudinal pores (130 nm diameter) completely interconnected via transverse nanochannels (of typically 50–70 nm diameter and around 530 nm in separation). This architecture differs fundamentally from conventional 1D-AAO templates; the 3D interconnected network permits complete infiltration of polymer in all spatial directions during hot-embossing, achieving complete pore infiltration, as confirmed by SEM cross-sections (see Figure S1).

2.1 | Structural Characterization

Beyond X_c, the rigid amorphous fraction (RAF) at crystal–amorphous interfaces dampens segmental mobility and increases interfacial scattering; RAF typically grows with imperfect/heterogeneous crystallization and can lower κ even when X_c is high. We therefore discuss κ using a three-parameter view: (i) chain orientation (f_c, per peak), (ii) X_c, and (iii) RAF/interphase quality.

PMMA serves as a critical control to isolate geometric and polymer disentanglement effects from crystallinity effects. PMMA (Figure 1a) remains completely amorphous in both bulk and confined states, with no crystalline reflections detected.

16136829, 0, Downloaded from https://onlinelibrary.wiley.com/doi/10.1002/smll.76561 by Karlsruher Institut Fur Technologie, Wiley Online Library on [13/11/2026]. See the Terms and Conditions (https://onlinelibrary.wiley.com/terms-and-conditions) on Wiley Online Library for rules of use; OA articles are governed by the applicable Creative Commons License

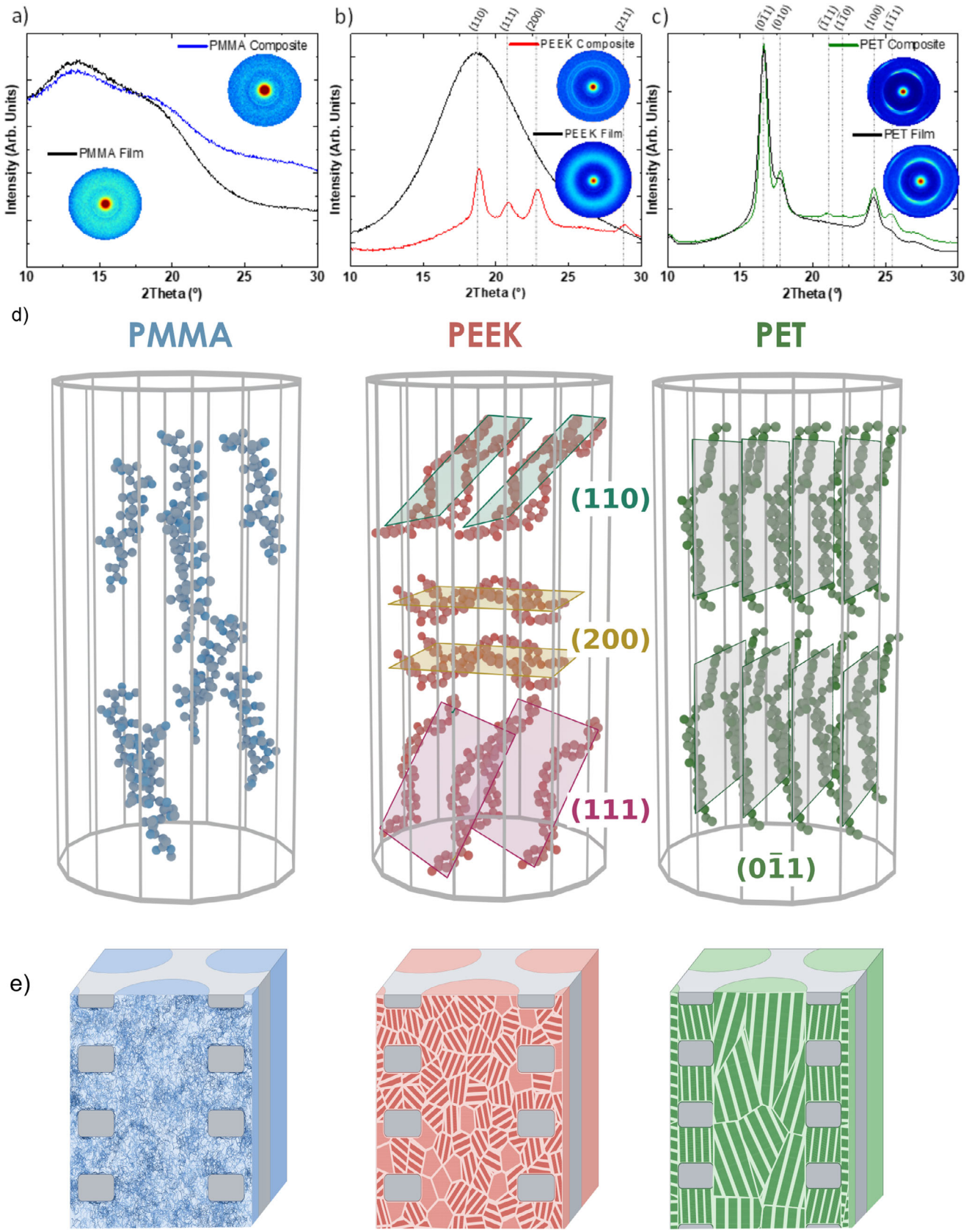


FIGURE 1 | 1D and 2D wide-angle X-ray scattering (WAXS) diffraction patterns of polymer/3D-AAO composites (colored lines) versus bulk reference samples (black lines) for (a) PMMA, (b) PEEK, and (c) PET. (d) Schematic illustration of the spatial orientation and conformation of polymer chains within the alumina nanopores, as inferred from the 2D-WAXS patterns of the three polymers infiltrated into ordered anodic aluminum oxide (AAO) channels viewed in cross-sectional perspective. (e) Schematic illustration (not to scale) of the polymers confined in the 3D-AAO nanopores (Ø ≈ 130 nm): amorphous PMMA, polycrystalline PEEK and semicrystalline PET aligned with the chain axis along the pore axis.

16136829, 0, Downloaded from https://onlinelibrary.wiley.com/doi/10.1002/smll.76561 by Karlsruher Institut Fur Technologie, Wiley Online Library on [13/11/2026]. See the Terms and Conditions (https://onlinelibrary.wiley.com/terms-and-conditions) on Wiley Online Library for rules of use; OA articles are governed by the applicable Creative Commons License

The absence of crystalline organization in PMMA establishes it as a benchmark for baseline geometric effects independent of crystallization. The 2D-WAXS pattern exhibits isotropic broad amorphous halos in both radial and azimuthal directions, confirming random 3D chain orientation without preferential crystallographic texture. Any enhancements in thermal and triboelectric properties in confined PMMA thus cannot be attributed to crystallization and are consistent with contributions from nanoconfinement geometry, polymer–alumina interfacial effects, and altered chain conformations and disentanglement.

PEEK, Figure 1b, demonstrates dramatic crystallization enhancement from completely amorphous bulk to 67.75% crystallinity upon 3D nanoconfinement. Strong crystalline reflections [(110), (111), (200), (211)] [16] are observed upon infiltration, indicating well-developed crystalline regions. Critically, these diffraction peaks emerge distributed across multiple azimuthal positions in the 2D-WAXS pattern, with no dominant meridional or equatorial concentration. This radial distribution indicates that crystalline domains within each cylindrical nanowire adopt random orientations rather than preferential alignment. The crystalline lamellae are oriented at numerous competing angles relative to the pore axis, creating a polycrystalline structure with abundant misoriented grain boundaries and high crystallite boundary density.

While the absolute crystallinity (67.75%) is substantial, the randomly oriented domains introduce multiple crystalline-amorphous interfaces with different crystallographic orientations. The mechanism producing random orientation in PEEK involves PEEK's complex crystallization kinetics: multiple competing nucleation sites on the 3D-AAO surface, combined with different growth rates for different crystalline faces of PEEK's orthorhombic unit cell, result in a kinetically trapped polycrystalline state rather than a thermodynamically preferred oriented state.

PET, Figure 1c, exhibits both increased crystallinity (74.1% vs. 70.0% bulk) and dramatically enhanced chain orientation. Strong crystalline reflections [$(0\bar{1}1)$ (010) (100)] for instance [17], are observed upon infiltration, indicating well-developed crystalline regions. Most remarkably, PET displays a concentrated meridional diffraction pattern, with diffraction intensity strongly localized at specific azimuthal positions. This meridional concentration is the fingerprint of uniaxial chain alignment. The Hermans orientation factor reaches $f_c = 0.915$, representing near-perfect uniaxial orientation along a single director.

The meridional diffraction pattern indicates that the crystalline structure in PET is organized with polymer chains (*c*-axis) preferentially aligned parallel to the cylindrical nanowire axis (Figure 1d). During hot-embossing infiltration at 255°C, the softened PET experiences pressure-driven flow through the cylindrical pores. This flow creates transient shear stress that extends polymer chains along the pore direction. Upon cooling post-infiltration, crystallization becomes kinetically restricted by the pore walls, allowing lamellae to grow preferentially in the geometrically favorable direction: with polymer chain axes parallel to the nanowire axis and crystalline lamellae stacked perpendicular to this axis. The cylindrical geometry physically constrains lamellar growth, promoting this single preferential orientation (Figure 1e). This is consistent with a strongly oriented crystalline texture, with the polymer chain axis preferentially aligned along the nanowire axis.

2.2 | Thermal Conductivity Enhancement: Comparative Role of Crystalline Texture and Disorder

Thermal conductivity measurements (detailed in Supporting Information) show different outcomes across the three polymers despite the common 3D nanoconfinement architecture (Figure 2a and Table 1). Using Effective Medium Theory (EMT) to extract polymer thermal conductivity (see Tables S1 and S2): PMMA achieves 0.90 ± 0.28 $W{\cdot}m^{-1}{\cdot}K^{-1}$ (350% enhancement vs. 0.20 $W{\cdot}m^{-1}{\cdot}K^{-1}$ bulk), PEEK shows 0.22 ± 0.20 $W{\cdot}m^{-1}{\cdot}K^{-1}$, which is not resolved from its bulk value of 0.25 $W{\cdot}m^{-1}{\cdot}K^{-1}$ within the propagated uncertainty, and PET reaches 1.17 ± 0.31 $W{\cdot}m^{-1}{\cdot}K^{-1}$ (290% enhancement vs. 0.30 $W{\cdot}m^{-1}{\cdot}K^{-1}$ bulk). These divergent outcomes, particularly the inverse ranking between PEEK (highest crystallinity increase, absence of thermal benefit) and PET (modest crystallinity increase, highest thermal benefit), indicate that absolute crystallinity enhancement (X_c) alone is not sufficient to explain the observed thermal conductivity changes. Within this dataset, the strong crystalline texture observed for PET is consistent with chain orientation being an important contributing factor to thermal conductivity.

PMMA, completely amorphous and incapable of crystallizing, serves as the essential control. Its 350% thermal enhancement ($0.20 \rightarrow 0.90$ $W{\cdot}m^{-1}{\cdot}K^{-1}$) cannot be attributed to crystallization. This result shows that confinement-related effects can substantially modify thermal transport in nanoconfined polymers even in the absence of crystalline order. The present data do not separately quantify the respective contributions of geometric confinement, chain disentanglement, polymer–alumina interfacial effects, and the EMT extraction itself, so these effects are discussed here as plausible contributors rather than as independently resolved mechanisms.

PEEK crystallizes dramatically upon nanoconfinement, increasing from completely amorphous bulk to 67.75% crystallinity (Figure 1b). Strong crystalline reflections [(110), (111), (200), (211)] emerge, indicating well-developed crystalline regions. Critically, the 2D-WAXS pattern reveals these crystalline domains distributed across multiple azimuthal positions with no dominant meridional or equatorial concentration, a clear fingerprint of polycrystalline disorder with randomly oriented domains rather than uniaxial alignment.

Despite this exceptional crystallinity increase (+67.75 percentage points), the slight variation in thermal conductivity (from 0.25 to 0.22 $W{\cdot}m^{-1}{\cdot}K^{-1}$) cannot be resolved within the propagated uncertainty from the bulk value of 0.25 $W{\cdot}m^{-1}{\cdot}K^{-1}$. This highlights the limitations of theoretical models like Ma & Tian's, which predict intrinsic crystalline thermal conductivity based on unit cell parameters. Within this dataset, high crystallinity (X_c) alone is not sufficient to guarantee a resolved thermal conductivity increase.

16136829, 0, Downloaded from https://onlinelibrary.wiley.com/doi/10.1002/smll.76561 by Karlsruher Institut Fur Technologie, Wiley Online Library on [13/11/2026]. See the Terms and Conditions (https://onlinelibrary.wiley.com/terms-and-conditions) on Wiley Online Library for rules of use; OA articles are governed by the applicable Creative Commons License

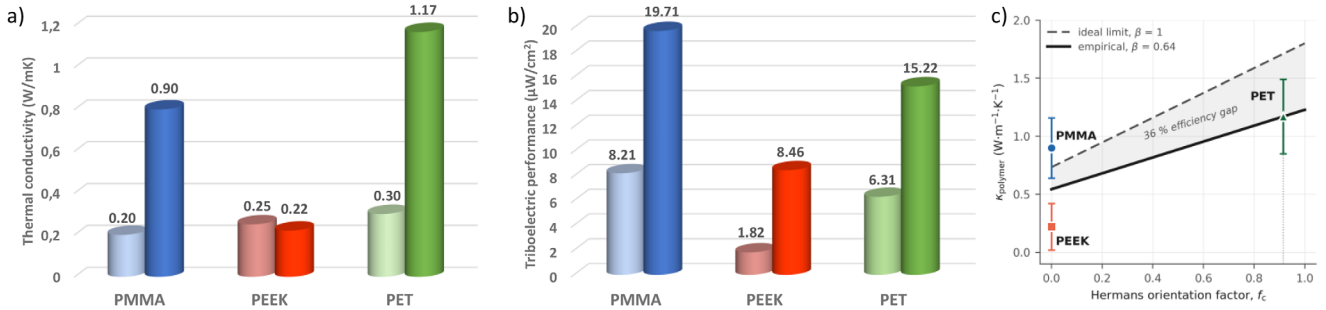


FIGURE 2 | a) Thermal conductivity of PMMA, PEEK, and PET in their bulk form (pale colored bars) compared with their nanostructured counterparts embedded in 3D-AAO templates (intense colored bars). Nanoconfinement increases conductivity by up to 350% (PMMA) and 290% (PET), whereas for PEEK the slight variation in thermal conductivity (from 0.25 to 0.22 $W \cdot m^{-1} \cdot K^{-1}$) cannot be resolved within the propagated uncertainty from the bulk value. b) Peak triboelectric power density for the same samples, showing 140% enhancement for PMMA (8.21 → 19.71 $\mu W \cdot cm^{-2}$), 365% for PEEK (1.82 → 8.46 $\mu W \cdot cm^{-2}$), and 141% for PET (6.31 → 15.22 $\mu W \cdot cm^{-2}$). c) Efficiency-Orientation Model (Equation 1) evaluated as a function of the Hermans orientation factor (f_c) using $\kappa_{amorph} = 0.2\ W \cdot m^{-1} \cdot K^{-1}$ and the ab-initio axial limit for PET, $\kappa_{TH} \approx 1.8\ W \cdot m^{-1} \cdot K^{-1}$. The dashed line is the ideal-transport limit ($\beta = 1$) and the solid line the empirical curve obtained from the PET data point ($\beta = 0.64$). The shaded area is the corresponding 36% efficiency gap. Plotted points are the EMT-extracted conductivities with their fully propagated uncertainties (Table S1). The efficiency factor $\beta = 0.64$ was obtained by fitting Equation (1) exclusively to the PET data point ($f_c = 0.915$); PMMA and PEEK are superimposed at $f_c = 0$ for visual reference and were not used in the fitting procedure. Their vertical displacement from the curve illustrates, rather than tests, the limits of the orientation-only description. Because κ_{TH} is specific to the PET crystal, the curves are quantitatively meaningful only for PET. PMMA and PEEK are shown at $f_c = 0$ for reference and the fact that they fall respectively above and below the orientation-only prediction illustrates that chain orientation alone does not determine the thermal conductivity in this dataset.

While PEEK's randomly oriented crystalline domains possess strong intramolecular covalent bonding, the misoriented grain boundaries between domains are expected to create acoustic impedance mismatch and phonon mode conversion. More broadly, paracrystalline disorder and the rigid amorphous fraction at heterogeneous interfaces are plausible sources of additional scattering. We therefore interpret the weak thermal response of confined PEEK as being consistent with substantial disorder-related scattering, while noting that the present study does not directly isolate the separate contributions of grain boundaries, intracrystalline defects, and interfacial regions.

PET achieves the highest absolute thermal conductivity (1.17 $W \cdot m^{-1} \cdot K^{-1}$, 290% enhancement) despite achieving only a modest crystallinity increase (69.98% bulk → 74.10% confined, ΔX_c = +4.12 percentage points), seemingly contradicting conventional understanding that crystallinity drives thermal transport. This apparent contradiction is consistent with crystalline texture being an important contributing factor: the Hermans orientation factor reaches $f_c = 0.915$, representing nearly perfect uniaxial alignment along the nanowire axis. Within this dataset, this strong texture is consistent with chain orientation contributing to the observed thermal enhancement, although polymer chemistry, confinement-related effects, and polymer–AAO interfacial coupling cannot be independently excluded.

2D-WAXS shows concentrated meridional diffraction intensity (Figure 1c), the fingerprint of uniaxial chain alignment. Strong crystalline reflections [$(0\bar{1}1)$ (010) (100)] are localized at specific azimuthal positions, indicating that polymer chains and crystalline lamellae are preferentially oriented with the chain backbone parallel to the cylindrical pore axis. During hot-embossing infiltration at 255°C, pressure-driven flow creates transient shear stress extending polymer chains along the pore direction. Upon cooling, the pore walls geometrically constrain lamellar growth, allowing crystallization to proceed preferentially with chains aligned parallel to the nanowire axis and lamellae stacked perpendicular to this axis. This represents extended-chain crystalline morphology consistent with enhanced thermal transport along the nanowire axis.

The near-perfect uniaxial orientation creates low-scattering thermal pathways along the polymer backbone through strong covalent C—C and C—O bonds. The crystalline domains, while only modestly increased (+4.12 percentage points), are uniformly oriented, minimizing the paracrystalline disorder that is expected to be more severe in PEEK. The crystalline–amorphous interfaces are therefore likely to be more organized than in the polycrystalline PEEK case. The combination of modest crystallinity increases and exceptional orientation ($f_c = 0.915$) is thus consistent with the large thermal enhancement observed for PET.

Rather than assigning numerical mean free paths to PET or PEEK, we limit the interpretation to the experimentally supported result: PET displays a larger EMT-extracted conductivity and a stronger crystalline texture than PEEK in the studied architecture. Determining whether thermal transport approaches a ballistic or quasi-ballistic regime and deconvolving the contributions of the AAO framework, polymer phase, and interphase would require temperature-dependent conductivity measurements, frequency-dependent TDTR, transient grating experiments [18], and coupled MD–finite-element modeling [19, 20]. Such characterization and modeling are beyond the scope of the present work.

This comparison shows that, within the studied architecture, crystallinity fraction alone without orientation (PEEK) does not capture the observed thermal response. The contrasting PET and PEEK results are consistent with crystalline texture and

16136829, 0, Downloaded from https://onlinelibrary.wiley.com/doi/10.1002/smll.76561 by Karlsruher Institut Fur Technologie, Wiley Online Library on [13/11/2026]. See the Terms and Conditions (https://onlinelibrary.wiley.com/terms-and-conditions) on Wiley Online Library for rules of use; OA articles are governed by the applicable Creative Commons License

TABLE 1 | Values for polymer and composite density (ρ), specific heat (C_p), and thermal conductivity (κ). $\rho_{polymer}$ and $C_{p,polymer}$ in this table correspond to the bulk/crystalline state.

Polymer	$\rho_{polymer}$ (g/cm^3)	$C_{p,polymer}$ (J/g·K)	$\rho_{composite}$ (g/cm^3)	$C_{p,composite}$ (J/g·K)	$\kappa_{bulk\ polymer}$ (W·m^{-1}·K^{-1})	$\kappa_{composite}$ (W·m^{-1}·K^{-1})	$\kappa_{polymer}$ (W·m^{-1}·K^{-1})
PMMA	1.09	1.47	1.75	1.11	0.20	1.01 ± 0.15	0.90 ± 0.28
PEEK	1.35	1.34	1.92	1.08	0.25	0.58 ± 0.09	0.22 ± 0.20
PET	1.35	1.11	1.92	0.98	0.30	1.18 ± 0.18	1.17 ± 0.31

disorder contributing to the EMT-extracted conductivity alongside polymer chemistry, confinement-related effects, and polymer–AAO interfacial coupling (see Table S3). These observations show that crystallinity fraction alone is insufficient to describe the thermal response of the present nanoconfined systems and that crystalline texture should be considered as an additional structural descriptor regarding thermal conductivity.

Confinement of heat-carrying vibrational modes provides an additional possible route by which nanoscale dimensions may modify thermal transport. Hydrodynamic-like phonon transport has been predicted for extremely thin crystalline nanowires, including Si nanowires at diameters of only a few nanometers [21]. Because the present systems are chemically and structurally different and have substantially larger diameters, this literature precedent cannot be directly extrapolated to our 3D-nanoconfined polymers. Our room-temperature, single-modulation-frequency measurements therefore provide no direct evidence for hydrodynamic phonon transport. Temperature-dependent and frequency-dependent thermal measurements would be required to test whether confinement of heat-carrying modes contributes to the observed conductivity.

This comparison demonstrates that the thermal transport bottleneck in these polymers is not described by absolute crystallinity alone. A polymer can crystallize abundantly yet provide little to no thermal benefit if that crystallization is accompanied by disorder and grain misorientation. Conversely, a modest crystallinity increase can coincide with substantial thermal enhancement when accompanied by strong chain alignment. Within this dataset, crystalline texture therefore emerges as a more informative descriptor than crystallinity alone.

In many inorganic materials, grain size and grain-boundary density can strongly influence thermal resistance, and increased crystalline order often improves heat transport. In semicrystalline polymers, however, crystallinity without directional order may coexist with paracrystalline disorder, crystalline–amorphous interfaces, and chain misalignment, all of which can increase phonon scattering. Relevant scattering sources may include local chain misorientation, boundaries between differently oriented crystallites, rigid-amorphous regions, and heterogeneous interphase structures. Therefore, within the present dataset, crystallinity fraction alone does not capture the thermal-transport response; crystalline texture and interphase quality must also be considered.

2.3 | Triboelectric Performance

Triboelectric measurements (Figure 2b) reveal nanoconfinement significantly amplifies power generation in all polymer-alumina composites. Under 1 N, 1 Hz contact-separation (22°C, 40% relative humidity) against 50 microns PTFE film, power densities are: PMMA 19.71 μW·cm^{-2} (140% enhancement over 8.21 μW·cm^{-2} bulk), PEEK 8.46 μW·cm^{-2} (365% enhancement over 1.82 μW·cm^{-2} bulk), and PET 15.22 μW·cm^{-2} (141% enhancement over 6.31 μW·cm^{-2} bulk). Thus, PEEK shows the largest relative enhancement, whereas PMMA shows the highest absolute power density among the nanostructured samples. As an example, detailed voltage–current characteristics and power densities *vs.* external load resistance (100 Ω to 470 MΩ) for PMMA (Figure S2), PEEK (Figure S3), and PET (Figure S4) provide the corresponding voltage, current, and instantaneous power-density dependence on external load reported in Figure 2b.

Because PMMA remains amorphous in both bulk and confined states, its 140% triboelectric enhancement cannot be attributed to crystallization. Instead, the result is consistent with a combination of architecture-, interface-, and dielectric-mediated effects associated with 3D nanoconfinement.

First, infiltration within the 3D-AAO template produces an interconnected PMMA nanonetwork, in which the longitudinal nanowires are joined by transverse polymer bridges. In contrast to an array of isolated 1D nanowires, these interconnections provide lateral continuity between neighboring polymer elements and create a 3D dielectric network. Such connectivity can reduce the spatial isolation of locally generated or trapped charges and modify their distribution, as well as the electric-field and polarization coupling throughout the nanostructure. In this sense, the transverse interconnections can provide shorter pathways between neighboring nanowires for charge redistribution and electrostatic coupling to the collecting electrode, rather than acting as conventional low-resistance conductive pathways.

Second, the very large internal PMMA–AAO interfacial area introduces an additional chemically and electronically heterogeneous interphase. Hydroxylated aluminum-oxide surfaces are known to interact directly with PMMA: the carbonyl groups of PMMA can form hydrogen bonds with surface Al–OH groups, while additional acid–base/ionic interactions may occur depending on the interfacial environment. These interactions can alter local chain conformation, interfacial polarization, and the energetic landscape for charge localization. Moreover, structural and oxygen-related defects in Al_2O_3 are known to introduce

16136829, 0, Downloaded from https://onlinelibrary.wiley.com/doi/10.1002/smll.76561 by Karlsruher Institut Fur Technologie, Wiley Online Library on [13/11/2026]. See the Terms and Conditions (https://onlinelibrary.wiley.com/terms-and-conditions) on Wiley Online Library for rules of use; OA articles are governed by the applicable Creative Commons License

electronic trapping states. Although the participation of specific AAO defect states in the present triboelectric response is not directly measured here, the large polymer–oxide interfacial area therefore provides a physically plausible additional contribution to charge localization and retention [22].

Third, the higher relative permittivity of alumina ($\varepsilon_r \approx 9$–10) [23] compared with PMMA increases the effective permittivity of the polymer/AAO composite (Table S4). For contact–separation TENGs, an increased dielectric permittivity can increase the effective capacitance and favor higher transferable/induced charge densities; this effect has been demonstrated previously for oxide–PMMA composites, including Al_2O_3–PMMA systems. The 3D architecture is particularly relevant here because it combines this dielectric contribution with an exceptionally large polymer–ceramic interfacial area.

The 140% enhancement observed for amorphous PMMA can therefore be rationalized by the combined influence of nanoscale contact geometry, 3D polymer connectivity, polymer–AAO interfacial interactions, defect-mediated charge localization, and increased effective permittivity. These contributions are physically consistent with the present 3D architecture, but they are not independently quantified by the measurements reported here; accordingly, we regard them as mutually compatible mechanisms contributing to the confinement-related baseline enhancement rather than assigning the observed increase to a single microscopic process.

Beyond its influence on the triboelectric response, the extensive polymer–AAO interface may also be relevant to thermal management during TENG operation. Repeated contact–separation involves dissipative processes, including interfacial friction, viscoelastic deformation, dielectric relaxation, charge dissipation, and resistive losses, which can dissipate part of the input mechanical energy and stored electrostatic energy as heat and generate local temperature rises during prolonged operation. Such temperature increases can in turn affect polymer mechanics, dielectric properties, and charge retention, establishing a bidirectional coupling between triboelectric performance and heat dissipation. In this context, the intimate PMMA–AAO contact produced by hot embossing may provide an additional route for removing locally generated heat from the polymer phase into the surrounding alumina framework. Vibrational mismatch at a polymer–ceramic interface can introduce thermal boundary resistance [24], whereas stronger interfacial interactions and intimate nanoscale contact can enhance vibrational energy transfer across the interface. For well-coupled polymer–oxide interfaces, thermal boundary resistances in the range of approximately 10^{-8} to 10^{-7} $m^2 \cdot K \cdot W^{-1}$ have been reported [8], and this range is used in the Supporting Information to bound the possible influence of the PMMA–AAO interface on thermal equilibration. We emphasize, however, that neither the interfacial thermal conductance nor the in-operando temperature rise is measured directly here; therefore, the present results establish the coexistence of enhanced triboelectric output and enhanced thermal transport in the 3D architecture, while improved dissipation of operationally generated heat remains a physically consistent implication rather than a directly demonstrated device-level mechanism.

PEEK shows the most significant triboelectric increase in relative terms (365%), greatly surpassing PMMA and PET enhancement. This ranking suggests that the polycrystalline disorder that is detrimental to thermal transport may, in this system, favor triboelectric performance through mechanisms related to charge generation and/or charge retention. Because these mechanisms are not directly measured here, they are presented below as plausible interpretations rather than as demonstrated causal pathways:

(1) The charge generation at the tips of nanowires is controlled by mechanics. PEEK's polycrystalline structure, which has randomly oriented crystalline domains with many grain boundaries, may be mechanically less resistant than PET's more oriented crystalline structure. Grain boundaries are weak areas in the structure. During PTFE contact–separation cycles, these weak grain boundaries could lower the mechanical energy barrier for covalent bond breakage at the nanowire tips. This process would not directly raise triboelectric charge density, but it could facilitate charge generation by easing bond scission during contact [14].

(2) Charge retention through interior grain boundary trapping: after charge is generated at the tips, the many grain boundaries inside polycrystalline PEEK may create a denser network of trapping sites than in PET. Multiscale modeling of charge transport in polymer composites shows that charges can accumulate in disordered interfacial areas where the site energy difference (ΔE_{ij}) between crystalline and amorphous domains creates energetic wells, and reduced electronic coupling (J_{ij}) hinders charge escape into ordered areas [25]. PEEK's random arrangement of crystalline domains is therefore consistent with a higher density of internal trapping sites than PET's more ordered lamellar structure.

(3) Better bonding between polymers and ceramics: the polymer chains at PEEK's grain boundaries are not aligned uniformly, so some segments may reorient to face the AAO cylindrical wall. This could increase the density of polymer–ceramic hydrogen-bonding sites (C═O···Al─OH interactions) compared with PET, where the chains are predominantly aligned parallel to the wall. This geometric effect, together with the extensive polymer–AAO contact area, could contribute to interfacial charge stabilization.

(4) Maxwell–Wagner–Sillars interfacial polarization: a collection of randomly oriented crystalline domains, each with its own dielectric response tensor, may yield a composite dielectric behavior with higher effective interfacial polarization than that of amorphous or highly aligned polymers. In that sense, the numerous internal interfaces in PEEK may behave as a distributed capacitive network that favors charge storage and retrieval.

PEEK's 365% triboelectric increase is therefore interpreted as being consistent with the synergistic effect of easier mechanical bond breakdown at the tips and improved charge retention inside the material. According to the quantified triboelectric series, PEEK is less tribonegative than PET (−76.25 *vs.* −89.44 μC/m^2), respectively [26] and therefore exhibits a larger difference in triboelectric charge density with respect to the PTFE counterlayer. However, this intrinsic ordering does not account for the observed behaiour, since bulk PEEK delivers the lowest power density of the three bulk references. This result indicates that

16136829, 0, Downloaded from https://onlinelibrary.wiley.com/doi/10.1002/smll.76561 by Karlsruher Institut Fur Technologie, Wiley Online Library on [13/11/2026]. See the Terms and Conditions (https://onlinelibrary.wiley.com/terms-and-conditions) on Wiley Online Library for rules of use; OA articles are governed by the applicable Creative Commons License

triboelectric performance in this system is not determined solely by intrinsic triboelectric charge density, but also by structural and interfacial factors [27].

It can then be concluded that PEEK's 365% triboelectric enhancement correlates with the abundance of crystalline–amorphous interfaces introduced by its polycrystalline structure. This suggests that disorder, which is detrimental to thermal transport, may be beneficial for triboelectric performance in this specific architecture.

PET exhibits a triboelectric enhancement of 141%, essentially identical to that of amorphous PMMA (140%) and substantially lower than that of PEEK (365%). This contrast indicates that the intrinsic position of a polymer in the triboelectric series does not uniquely determine the relative power enhancement obtained upon nanoconfinement. Compared with polycrystalline PEEK, PET develops a strongly oriented crystalline morphology (f_c = 0.915) with fewer randomly oriented crystalline domains and heterogeneous crystalline–amorphous boundaries. Such a more ordered morphology may provide fewer structurally heterogeneous regions capable of promoting charge localization or interfacial polarization, while its greater structural order may also reduce mechanically assisted bond-scission processes during contact. These effects are consistent with the smaller relative enhancement observed for PET compared with PEEK; however, trap density, bond-scission probability, dielectric relaxation, and charge mobility were not independently measured here. The PET–PEEK comparison is therefore interpreted as a correlation between microstructural order and triboelectric response rather than as evidence for a direct dependence of triboelectric performance on the Hermans orientation factor or for a unique microscopic charge-transport mechanism.

A summary of the results obtained is provided in Table 2, whereas a summary of the main conclusions can be found in Table 3. Our data support a three-parameter view of κ (orientation (f_c), X_c, and RAF/interphase quality) with crystalline texture emerging as a key descriptor within this dataset. For triboelectricity, these 3D composites behave as interfacial-dominated dielectrics, where internal interfaces and charge-trapping processes plausibly influence the output ranking.

2.4 | Structure-Property Relationships

The simultaneous characterization of thermal conductivity and triboelectric power generation reveals distinct and, in some cases, opposing structure–property trends under 3D nanoconfinement. These contrasting responses arise from the interplay of nanoscale architectural effects, as elucidated by the comparative data in Tables 2 and 3.

This highlights the limitations of theoretical models like Ma & Tian's [9], which predict intrinsic crystalline thermal conductivity based on unit cell parameters. While these frameworks, along with ab initio anharmonic lattice dynamics calculations by Utimula et al. [28], provide essential intrinsic upper bounds (predicting for instance, an axial limit of $\kappa \approx$ 1.8 W·m^{-1}·K^{-1} for perfect PET crystals), they inherently neglect the mesoscopic disorder and misorientation characterizing synthesized polymer systems. Therefore, comparing our experimental value (κ_{exp} = 1.17 W·m^{-1}·K^{-1}) directly to ideal predictions underscores the need to incorporate crystalline texture and disorder into the discussion of thermal transport [9, 28].

To rationalize the discrepancy between the theoretical lattice limit and our measured values, we propose an "Efficiency-Orientation Model". This model interpolates between the amorphous conductivity limit (κ_{amorph}) and the ideal oriented-crystal limit (κ_{TH}), weighted by the geometric projection of the polymer backbone along the heat-flow axis (z) and a phenomenological scattering-efficiency factor. Following the tensor derivation detailed in the Supporting Information, we formulate the refined thermal conductivity, $\kappa_{refined}$, as:

$$\kappa_{refined} = \kappa_{amorph} + \beta \cdot (\kappa_{TH} - \kappa_{amorph}) \cdot \left(\frac{2 \cdot f_c + 1}{3} \right) \quad (1)$$

where, κ_{TH} represents the theoretical intrinsic upper limit of the perfect crystal and $\kappa_{\text{amorph}} \approx$ 0.2 W·m^{-1}·K^{-1} represents its counterpart; the lower limit of the amorphous state of the polymer. Here, the bracketed term $\left[\frac{2 \cdot f_c + 1}{3}\right]$ represents the geometric correction factor derived from the Hermans orientation function (f_c), projecting the anisotropic backbone conductivity onto the measurement axis (see Supporting Information for derivation). Crucially, we introduce the parameter ($0 < \beta \leq 1$) as a phenomenological efficiency factor. While f_c quantifies alignment, β quantifies the quality of the phonon transport path. In the present manuscript, β is used only as an empirical fitting parameter that captures the impact of disorder-related scattering in a phenomenological manner; it is not an independently measured physical quantity.

Applying this model to our nanoconfined PET nanowires (κ_{exp} = 1.17 W/m·K, f_c = 0.915) and assuming the theoretical intrinsic maximum of $\kappa_{TH} \approx$ 1.8 W/m·K, we extract an efficiency factor of $\beta \approx$ 0.64. This result provides a compact phenomenological description of the thermal enhancement: nanoconfinement-induced near-perfect uniaxial chain alignment (high f_c), effectively creating crystalline bridges for heat flow, yet the transport efficiency remains below the theoretical maximum. We therefore interpret β as a descriptor of the residual reduction relative to the ideal oriented-crystal limit, without assigning it a unique microscopic origin (Figure 2c).

It is nevertheless instructive to consider which physical processes are included into the 36% underperformance that β represents. Even at f_c = 0.915, an infiltrated nanowire is not a single extended crystal: the finite molecular weight of the polymer imposes a finite density of chain ends, each of which terminates a covalent transport pathway. Point defects and conformational bends within the crystalline branches introduce mass and force-constant disorder that scatters the high-frequency modes carrying most of the heat; and the rigid amorphous fraction at the crystalline-amorphous boundaries, which is expected to be substantial under confinement, interposes weakly bonded, van der Waals-mediated segments in series with the covalent pathway. Interfacial resistance between the polymer and the pore walls acts in the same direction. We highlight that our measurements do not resolve these contributions individually, and β should therefore

16136829, 0, Downloaded from https://onlinelibrary.wiley.com/doi/10.1002/smll.76561 by Karlsruher Institut Fur Technologie, Wiley Online Library on [13/11/2026]. See the Terms and Conditions (https://onlinelibrary.wiley.com/terms-and-conditions) on Wiley Online Library for rules of use; OA articles are governed by the applicable Creative Commons License

TABLE 2 | Comparative Analysis of 3D Nanoconfinement Effects on Semicrystalline vs. Amorphous Polymers. † Indicates values derived from interpretation of WAXS data and structure analysis.

Parameter	PMMA (Amorphous)	PEEK (Semicrystalline)	PET (Semicrystalline)
Bulk crystallinity (%)	N/A	0.0	69.98
Confined crystallinity (%)	N/A	67.75	74.10
Δ Crystallinity (%)	N/A	+67.75	+4.12
Grain boundary density†	Low (no grains)	High (random polycrystalline)	Low (aligned)
Dominant chain orientation†	None	Random	Uniaxial
Hermans orientation factor (f_c)	N/A	0	0.915
Plausible structural contribution to thermal scattering†	Chain disorder/entanglement	Misoriented crystallites and heterogeneous boundaries	Reduced orientational disorder
Thermal conductivity (bulk, W/m·K)	0.20	0.25	0.30
Thermal conductivity (confined 3D, W/m·K)	0.90 ± 0.28	0.22 ± 0.20	1.17 ± 0.31
Δ Thermal conductivity (%)	350	Not resolved within the propagated uncertainty	290
Triboelectric power enhancement (%)	140	365	141

TABLE 3 | Summary of the antagonistic structure–property relationships in 3D-nanoconfined polymers. The descriptors indicate how structural motifs associated with efficient thermal transport may simultaneously oppose the disorder-related mechanisms that can enhance triboelectric output in this architecture.

Structure factor	Thermal conductivity (κ)	Triboelectric power density (P)
Chain Orientation (f_c)	Promoting/Modulating: Strong orientation can provide preferential heat-transport pathways along the pore axis when combined with sufficiently low structural disorder.	Indirect/Modulating: Strongly ordered and oriented morphologies may contain fewer heterogeneous regions for charge localization and may alter the mechanical response during contact. No direct dependence of triboelectric performance on (f_c) is established here.
Crystalline grain boundaries	Potentially inhibitory: Misorientation between neighboring crystallites and the associated disordered interphases can increase scattering of heat-carrying vibrational modes and interrupt preferential thermal-transport pathways.	Potentially beneficial: Grain boundaries and their associated disordered regions may provide structurally and energetically heterogeneous sites that favor charge localization or retention.
Polycrystalline disorder	Potentially suppressive: Randomly oriented crystallites, grain boundaries, and heterogeneous interphases can increase vibrational scattering and reduce the benefit expected from a high crystalline fraction.	Potentially beneficial: Increased structural and dielectric heterogeneity may favor charge localization and interfacial polarization, providing a possible contribution to the enhanced relative triboelectric response.
Heterogeneous interfaces / defect-related trapping states	Potentially resistive: Structural disorder and imperfect vibrational coupling at interfaces can introduce additional thermal resistance and scattering.	Potentially beneficial: Interfacial or defect-related trapping states can contribute to charge retention and reduce charge decay; however, the specific trapping states involved are not directly identified in the present study.

16136829, 0, Downloaded from https://onlinelibrary.wiley.com/doi/10.1002/smll.76561 by Karlsruher Institut Fur Technologie, Wiley Online Library on [13/11/2026]. See the Terms and Conditions (https://onlinelibrary.wiley.com/terms-and-conditions) on Wiley Online Library for rules of use; OA articles are governed by the applicable Creative Commons License

be read as their aggregate phenomenological signature rather than as a quantity attributable to any single mechanism.

3 | Conclusions

Our systematic comparison of PMMA, PEEK, and PET within the same interconnected 3D-AAO nanoarchitecture shows that crystallinity, crystalline texture, microstructural disorder, and interfacial structure do not contribute equivalently to thermal and triboelectric behavior under nanoconfinement. PET combines only a modest increase in crystallinity (+4.12 percentage points) with a strongly oriented crystalline texture (f_c = 0.915) and exhibits the highest absolute EMT-extracted thermal conductivity of the confined polymers (1.17 ± 0.31 W m^{-1} K^{-1}). In contrast, PEEK develops a high crystalline fraction (67.75%) but remains strongly polycrystalline, and its thermal conductivity is similar and not resolved from that of the bulk reference within the propagated uncertainty. PMMA remains completely amorphous yet exhibits the largest relative thermal-conductivity increase with respect to its own bulk reference (+350%). Together, these observations demonstrate that crystallinity fraction alone is an incomplete descriptor of thermal transport in nanoconfined polymers: crystalline texture, orientational disorder, confinement, and polymer–interface effects must also be considered.

The contrast between PET and PEEK is particularly relevant for polymer thermal transport. Strong crystalline texture is associated here with efficient heat transport along the confinement direction, whereas a large crystalline fraction without preferential orientation does not produce a resolved conductivity enhancement. This distinction suggests that quantitative descriptors of orientation and microstructural disorder should complement crystallinity when analyzing and modelling heat transport in semicrystalline polymers. The Efficiency–Orientation Model introduced here provides a phenomenological framework for describing this contribution of crystalline texture, while the behavior of PMMA emphasizes that confinement-related and interfacial contributions remain important even in the complete absence of crystallization.

Triboelectric behavior follows a different structural trend. The relative power-density enhancement is PEEK (365%) > PET (141%) ≈ PMMA (140%), whereas the absolute nanostructured power density follows PMMA (19.71 μW·cm^{-2}) > PET (15.22 μW·cm^{-2}) > PEEK (8.46 μW·cm^{-2}). The particularly large relative enhancement of polycrystalline PEEK is consistent with microstructural heterogeneity playing a role beyond the intrinsic triboelectric affinity of the polymer. Grain boundaries and crystalline–amorphous interfaces may influence mechanically assisted charge generation, charge localization, and interfacial polarization, although these microscopic processes were not independently resolved in the present experiments. The results therefore identify microstructural heterogeneity as a potentially useful additional variable for interpreting and engineering triboelectric polymer systems, rather than establishing a direct dependence on crystalline orientation itself.

A central outcome of this work is therefore that the structural motifs associated with efficient thermal transport and those associated with enhanced triboelectric response are not necessarily the same. Within the present platform, strong crystalline texture and reduced orientational disorder are associated with efficient heat transport, whereas the largest relative triboelectric enhancement occurs in the more heterogeneous polycrystalline morphology. At the same time, the substantial thermal and triboelectric enhancements observed for amorphous PMMA demonstrate that the interconnected 3D architecture itself, including nanoscale geometry, polymer–AAO interfacial interactions, dielectric effects, and 3D polymer connectivity, provides an important contribution independent of crystallization. These results show that no single structural parameter can be expected to optimize both functionalities simultaneously.

This distinction has direct implications for the design of multifunctional polymer materials. For thermal management, processing strategies should consider not only increasing crystallinity but also promoting directional crystalline texture while limiting disorder that interrupts heat-transport pathways. For triboelectric energy harvesting, controlled microstructural heterogeneity and internal interfaces may offer additional routes for enhancing relative output, although their individual contributions should be isolated within a single polymer before general design rules are established. When thermal dissipation and triboelectric energy harvesting must coexist, optimization should therefore be treated as a multidimensional structural problem rather than as the maximization of crystallinity, dielectric response, or triboelectric affinity independently.

More broadly, the 3D-AAO platform provides a controlled route for separating and comparing structural descriptors that are normally coupled during conventional polymer processing. By revealing that crystalline texture provides information beyond crystallinity fraction for thermal transport, while microstructural heterogeneity appears relevant to triboelectric enhancement, this work establishes a framework for connecting polymer morphology with two technologically important but rarely examined functionalities within the same nanoscale architecture. Future experiments that independently vary orientation, crystallinity, and interfacial morphology within a single polymer will be essential to transform these correlations into predictive design rules for thermally managed triboelectric and other multifunctional polymer nanostructures.

4 | Experimental Section

4.1 | 3D-AAO Template Fabrication in Oxalic Acid

The oxalic-acid 3D-AAO architecture with interlinks between vertical pores matches prior reports on interconnected 3D-AAO fabricated by pulsed/current-modulated anodization; such interlinks promote 3D infiltration and anisotropic alignment/kinetic selection.

The ordered 3D-AAO templates [29] were fabricated by one-step current-pulsed anodization [30] in oxalic acid [31]. High-purity aluminum sheet (99.999%, Advent Research Materials) was cleaned by sonication in acetone, water, isopropanol, and ethanol for 5 min in each solvent to remove some organic

16136829, 0, Downloaded from https://onlinelibrary.wiley.com/doi/10.1002/smll.76561 by Karlsruher Institut Fur Technologie, Wiley Online Library on [13/11/2026]. See the Terms and Conditions (https://onlinelibrary.wiley.com/terms-and-conditions) on Wiley Online Library for rules of use; OA articles are governed by the applicable Creative Commons License

TABLE 4 | Infiltration conditions for each polymer.

Polymer	PMMA	PEEK	PET
Working temperature (°C)	160	348	255
Cooling Time (min)	6	14	9
Pressing Time (s)	180	60	60

impurities. After that, the foil was electropolished in a solution of perchloric acid with ethanol (1:3) under 20 V for 2 min. Then, the anodization process was carried out using 0.3 M oxalic acid (99%, Sigma–Aldrich) solution as the electrolyte at −1°C. The process developed for oxalic acid comprised 50 pulses, in which the current values were 13.3 mA/cm^2 for the high current stage for 80 s and 1.1 mA/cm^2 for the low current stage for 400 s. To provide the structure with mechanical stability, a constant high current density should be applied during 300 s to grow the first 1D-AAO layer.

Post-anodization treatment involved 5 *wt.*% H_3PO_4 at 30°C for 60 min to open transversal nanochannels and create the complete 3D network architecture essential for obtaining the 3D polymer networks.

4.2 | Hot-Embossing Infiltration Process

Polymeric 3D nanonetworks of poly(methyl methacrylate) (PMMA), polyetheretherketone (PEEK), and polyethylene terephthalate (PET) were fabricated via hot embossing [32]. We place it over the 3D-AAO between two Kapton sheets. Then, the mold was heated to a certain temperature (see Table 4) before stabilizing at the desired working temperature. Once the system is stable at the molding temperature for 60 s, a force of 25 kN is applied to fill the 3D template with the polymer. In the present protocol, cooling was performed under a single fixed condition following infiltration, which precluded generating a range of f_c values within the same polymer in this study. We note that the hot-embossing platform itself does not preclude such variation: post-infiltration cooling-rate control (e.g., staged or gradient post-cooling after demolding) is a feasible extension of the technique and represents the most direct route to decouple chain orientation from polymer identity in future work, by processing a single polymer (e.g., PET) across a controlled series of f_c values.

After the infiltration process, the underlying aluminum was removed using an aqueous solution of $CuCl_2$/HCl, and the barrier layer grown during the anodization process was also removed using a 10 *wt.*% H_3PO_4 solution at 30°C for 10 min.

4.3 | Advanced Characterization

The morphological characterization of 3D-AAO nanostructures was studied using high-resolution Scanning Electron Microscopy (HR-SEM, FEI Verios 460). The observation was performed under low current and voltage settings with fast image acquisition (conditions of 13 pA and 1.3 kV, respectively). For the polymeric samples, 5 nm of chrome were deposited on the nanostructures before SEM imaging.

The crystal phases of 3D nanocomposites were determined by wide-angle X-ray scattering (WAXS) in SAXSpoint 5.0 (Anton Paar), equipped with a Cu Kα microfocus source (λ = 1.5418 Å) and using a 2D Pilatus 1 M (Dectris) detector that allows us to analyze the preferred directions in the formation of polymer crystals. 2D patterns were converted into 1D intensity profiles using the SAXS analysis software. The degree of molecular orientation was estimated from the azimuthal intensity distribution $I(\varphi)$ of the main diffraction peak. The azimuthal intensity profile is used to calculate the Hermans orientation factor (f_c), which is 0 for a fully isotropic structure and 1 for a perfect uniaxial orientation.

The thermal conductivity of the samples was determined using a picosecond thermoreflectance (PicoTR) apparatus. Measurements were performed in a Front-Front configuration, employing a 775 nm probe laser and a 1550 nm pump laser. To optimize both the reflectance of the probe beam and the absorptance of the pump beam at the sample surface, a 100 nm platinum transducer layer was deposited prior to the measurement. The phase shift between the reference and reflected probe beams was recorded. The resulting experimental curve was subsequently fitted to obtain the effective thermal conductivity of the polymer/3D-AAO composite. The thermal conductivity of the confined polymer phase was then derived using the effective-medium analysis described in the Supporting Information [33, 34]. The thermal diffusion length was estimated as $\delta = \sqrt{\frac{\alpha}{\pi f}}$; with $\alpha \approx (0.3 - 0.8)$ mm^2·s^{-1} and $f = 20$ MHz, $\delta \approx 70$–110 nm, i.e., comparable to the pore diameter (130 nm); the measurement therefore probes the near-surface region of the polymer/3D-AAO composite, laterally averaged over the pores within the laser spot.

Tribo-Electric Measurement System Model HO-TBM-02 was used to perform the contact and separation of triboelectric pairs setting the force at 1 N at 1 Hz of frequency (22°C, 40% relative humidity). The plate with the positive tribo-material is movable to meet the negative tribo-material (50 μm film of Polytetrafluoroethylene), which is in the static plate. The voltage and current were measured using a programmable electrometer (Keithley 6514). Real-time acquisition and control were performed with lab-made control software built with LabVIEW. The samples were attached to a double-sided copper tape that was pasted onto the other side to a glass. This copper tape also has a welded cable to collect the generated charges.

Author Contributions

Carlos G. Cobos: investigation, validation, visualization, Writing – review and editing, Writing – original draft, formal analysis. **Miguel Ángel Tenaguillo**: investigation, writing – original draft, formal analysis. **Diego Garay-Ruiz**: visualization. **Matthias Worgull**: methodology. **Marc Schneider**: methodology. **Juan P. Fernández-Blázquez**: methodology, visualization, investigation. **Marisol Martin-Gonzalez**: conceptualization, investigation, funding acquisition, writing – original draft, writing – review and editing, validation, formal analysis, project administration, supervision.

16136829, 0, Downloaded from https://onlinelibrary.wiley.com/doi/10.1002/smll.76561 by Karlsruher Institut Fur Technologie, Wiley Online Library on [13/11/2026]. See the Terms and Conditions (https://onlinelibrary.wiley.com/terms-and-conditions) on Wiley Online Library for rules of use; OA articles are governed by the applicable Creative Commons License

Acknowledgements

The authors acknowledge financial support from "ERC Advanced Grant Number. 101052603, PowerbyU". We acknowledge the service from the MiNa Laboratory at IMN. Open access publication fees were covered by the Consejo Superior de Investigaciones Científicas (CSIC).

Conflicts of Interest

The authors declare no conflicts of interest.

Data Availability Statement

The data that support the findings of this study are available from the corresponding author upon reasonable request.

References

1. Y. Dong, Y. Feng, and D. Wang, "A High-Performance Triboelectric Nanogenerator With Dual Nanostructure for Remote Control of Switching Circuit," *Chemical Science* 15 (2024): 10436–10447, https://doi.org/10.1039/D4SC01432D.

2. D. Choi, Y. Lee, Z. H. Lin, et al., "Recent Advances in Triboelectric Nanogenerators: From Technological Progress to Commercial Applications," *ACS Nano* 17 (2023): 11087–11219, https://doi.org/10.1021/acsnano.2c12458.

3. S. Bairagi, S. Banerjee, C. Shee, et al., "Polyethyleneimine (PEI)-Treated Multifunctional Textile Triboelectric Nanogenerator: A Scalable and Cost-Effective Solution for Self-Powered Electronics, Energy Harvesting and Physiological Movement Monitoring," *Nano Energy* 139 (2025): 110990, https://doi.org/10.1016/j.nanoen.2025.110990.

4. Q. Shao, C. Pei, M. Jin, Y. Ding, Z. Chen, and T. Kuang, "Anchoring Nanofillers at Immiscible Polymer Interfaces Enables Strong, Tough, High-Output Triboelectrics," *Nano Letters* 25 (2025): 15895–15903, https://doi.org/10.1021/acs.nanolett.5c04196.

5. Y. Zhao, R. Wu, Y. Hao, et al., "Eco-Friendly Multifunctional Hydrogel Sensors Enabled Sustainable and Accurate Human-Machine Interaction System," *Advanced Materials* 37 (2025): 2507127, https://doi.org/10.1002/adma.202507127.

6. H. Chen, V. V. Ginzburg, J. Yang, et al., "Thermal Conductivity of Polymer-Based Composites: Fundamentals and Applications," *Progress in Polymer Science* 59 (2016): 41–85, https://doi.org/10.1016/j.progpolymsci.2016.03.001.

7. S. Ghaffari-Mosanenzadeh, O. Aghababaei Tafreshi, E. Dammen-Brower, E. Rad, M. Meysami, and H. E. Naguib, "A Review on High Thermally Conductive Polymeric Composites," *Polymer Composites* 43 (2022): 692–711, https://doi.org/10.1002/pc.26420.

8. H. Ma, K. Lionti, T. P. Magbitang, et al., "Pore-Confined Polymers Enhance the Thermal Conductivity of Polymer Nanocomposites," *ACS Macro Letters* 11 (2022): 116–120, https://doi.org/10.1021/acsmacrolett.1c00703.

9. H. Ma, Y. Ma, and Z. Tian, "Simple Theoretical Model for Thermal Conductivity of Crystalline Polymers," *ACS Applied Polymer Materials* 1 (2019): 2566–2570, https://doi.org/10.1021/acsapm.4c03165.

10. V. Singh, T. L. Bougher, A. Weathers, et al., "High Thermal Conductivity of Chain-Oriented Amorphous Polythiophene," *Nature Nanotechnology* 9 (2014): 384–390, https://doi.org/10.1038/nnano.2014.44.

11. Y. Nie, H. Gao, M. Yu, Z. Hu, G. Reiter, and W. Hu, "Competition of Crystal Nucleation to Fabricate the Oriented Semi-Crystalline Polymers," *Polymer* 54 (2013): 3402–3407, https://doi.org/10.1016/j.polymer.2013.04.047.

12. M. Schulz, M. Schäfer, K. Saalwächter, and T. Thurn-Albrecht, "Competition Between Crystal Growth and Intracrystalline Chain Diffusion Determines the Lamellar Thickness in Semicrystalline Polymers," *Nature Communications* 13 (2022): 119, https://doi.org/10.1038/s41467-021-27752-0.

13. C. G. Cobos, C. Rodrigues, M. M. Ramos, J. Ventura, A. M. Pereira, and M. Martín-González, "Enhanced Energy Harvesting Performance of Biodegradable Polylactic Acid/3D Anodic Aluminum Oxide Composite Triboelectric Nanogenerators," *Advanced Electronic Materials* 12 (2026): 00237, https://doi.org/10.1002/aelm.202500237.

14. O. Verners, L. Lapčinskis, P. C. Sherrell, and A. Šutka, "Contact Electrification at Dielectric Polymer Interfaces: On Bond Scission, Material Transfer, and Electron Transfer," *Advanced Materials Interfaces* 10 (2023): 2300562, https://doi.org/10.1002/admi.202300562.

15. Y. Nan, J. Shao, M. Willatzen, and Z. L. Wang, "Understanding Contact Electrification at Water/Polymer Interface," *Research* 2022 (2022): 9861463, https://doi.org/10.34133/2022/9861463.

16. C. Fougnies, P. Damman, M. Dosière, and M. H. J. Koch, "Time-Resolved SAXS, WAXS, and DSC Study of Melting of Poly(Aryl Ether Ether Ketone) (PEEK) Annealed from the Amorphous State," *Macromolecules* 30, no. 5 (1997): 1392–1399, https://doi.org/10.1021/ma961151i.

17. Z.-G. Wang, B. S. Hsiao, B. X. Fu, et al., "Correct Determination of Crystal Lamellar Thickness in Semicrystalline Poly(Ethylene Terephthalate) by Small-Angle X-Ray Scattering," *Polymer* 41 (2000): 1791–1797, https://doi.org/10.1016/S0032-3861(99)00327-4.

18. A. B. Robbins, S. X. Drakopoulos, I. Martin-Fabiani, S. Ronca, and A. J. Minnich, "Ballistic Thermal Phonons Traversing Nanocrystalline Domains in Oriented Polyethylene," *Proceedings of the National Academy of Sciences* 116 (2019): 17163–17168, https://doi.org/10.1073/pnas.1905492116.

19. H. Fan, Z. Li, and Y. Zhou, "Influence of Adsorbed Gas Molecules on Thermal Transport in Metal-Organic Framework HKUST-1," *Physical Review Applied* 23 (2025): 054006, https://doi.org/10.1103/PhysRevApplied.23.054006.

20. Q. He, Y. Chen, Z. Li, and Y. Zhou, "Unveiling the Ultralow Thermal Conductivity of Hybrid Perovskites," *Advanced Science* 13 (2026): 76841, https://doi.org/10.1002/advs.76841.

21. Y. Zhou, X. Zhang, and M. Hu, "Nonmonotonic Diameter Dependence of Thermal Conductivity of Extremely Thin Si Nanowires: Competition Between Hydrodynamic Phonon Flow and Boundary Scattering," *Nano Letters* 17 (2017): 1269–1276, https://doi.org/10.1021/acs.nanolett.6b05113.

22. S. Pletincx, K. Marcoen, L. Trotochaud, et al., "Unravelling the Chemical Influence of Water on the PMMA/Aluminum Oxide Hybrid Interface In Situ," *Scientific Reports* 7 (2017): 13341, https://doi.org/10.1038/s41598-017-13549-z.

23. Y. J. Kim, J. Lee, S. Park, C. Park, and C. Park, "Effect of the Relative Permittivity of Oxides on the Performance of Triboelectric Nanogenerators," *RSC Advances* 7 (2017): 49368–49373, https://doi.org/10.1039/C7RA07274K.

24. J. Gu and K. Ruan, "Breaking Through Bottlenecks for Thermally Conductive Polymer Composites: A Perspective for Intrinsic Thermal Conductivity, Interfacial Thermal Resistance and Theoretics," *Nanomicro Letters* 13 (2021): 110, https://doi.org/10.1007/s40820-021-00640-4.

25. T. Cheng, H. Hu, N. Valizadeh, et al., "The Influence of Discontinuity-Induced Fringing Effect on the Output Performance of Contact-Separation Mode Triboelectric Nanogenerators: Experiment and Modeling Studies," *Advanced Energy and Sustainability Research* 5 (2024): 2470027, https://doi.org/10.1002/aesr.202470027.

26. H. Zou, Y. Zhang, L. Guo, et al., "Quantifying the Triboelectric Series," *Nature Communications* 10 (2019): 1427, https://doi.org/10.1038/s41467-019-09461-x.

27. K. Shi, B. Chai, H. Zou, et al., "Contact Electrification at Adhesive Interface: Boosting Charge Transfer for High-Performance Triboelectric Nanogenerators," *Advanced Functional Materials* 33 (2023): 2307678, https://doi.org/10.1002/adfm.202307678.

28. K. Utimula, T. Ichibha, R. Maezono, and K. Hongo, "Ab Initio Search of Polymer Crystals With High Thermal Conductivity," *Chemistry of Materials* 31 (2019): 4649–4656, https://doi.org/10.1021/acs.chemmater.9b00020.

16136829, 0, Downloaded from https://onlinelibrary.wiley.com/doi/10.1002/smll.76561 by Karlsruher Institut Fur Technologie, Wiley Online Library on [13/11/2026]. See the Terms and Conditions (https://onlinelibrary.wiley.com/terms-and-conditions) on Wiley Online Library for rules of use; OA articles are governed by the applicable Creative Commons License

29. M. Martín-González, "3D Anodic Alumina Nanoarchitectures: A Decade of Progress from Foundational Science to Functional Metamaterials," *Advanced Materials* 38 (2026): 14821, https://doi.org/10.1002/adma.202514821.

30. P. M. Resende, R. Sanz, O. Caballero-Calero, and M. Martín-González, "Cost-Effective, Flexible, Hydrophobic, and Tunable Structural Color Polymeric Bragg Reflector Metastructures," *Advanced Optical Materials* 6 (2018): 1800408, https://doi.org/10.1002/adom.201800408.

31. J. Martín, C. V. Manzano, and M. Martín-González, "In-Depth Study of Self-Ordered Porous Alumina in the 140–400 nm Pore Diameter Range," *Microporous and Mesoporous Materials* 151 (2012): 311–316, https://doi.org/10.1016/j.micromeso.2011.10.018.

32. M. Worgull, A. Kolew, M. Heilig, M. Schneider, H. Dinglreiter, and B. Rapp, "Hot Embossing of High Performance Polymers," *Microsystem Technologies* 17 (2011): 585–592, https://doi.org/10.1007/s00542-010-1155-0.

33. B. Abad, J. Maiz, A. Ruiz-Clavijo, O. Caballero-Calero, and M. Martin-Gonzalez, "Tailoring Thermal Conductivity via Three-Dimensional Porous Alumina," *Scientific Reports* 6 (2016): 38595, https://doi.org/10.1038/srep38595.

34. B. Abad, J. Maiz, and M. Martin-Gonzalez, "Rules to Determine Thermal Conductivity and Density of Anodic Aluminum Oxide (AAO) Membranes," *The Journal of Physical Chemistry C* 120 (2016): 5361–5370, https://doi.org/10.1021/acs.jpcc.6b00643.

Supporting Information

Additional supporting information can be found online in the Supporting Information section.

Supporting File: smll76561-sup-0001-SuppMat.docx.

16136829, 0, Downloaded from https://onlinelibrary.wiley.com/doi/10.1002/smll.76561 by Karlsruher Institut Fur Technologie, Wiley Online Library on [13/11/2026]. See the Terms and Conditions (https://onlinelibrary.wiley.com/terms-and-conditions) on Wiley Online Library for rules of use; OA articles are governed by the applicable Creative Commons License